Miner Deposita (2006) 41: 229–245
DOI 10.1007/s00126-006-0057-7

ARTICLE

Karen Rickers · Rainer Thomas · Wilhelm Heinrich

The behavior of trace elements during the chemical evolution of the H_2O-, B-, and F-rich granite–pegmatite–hydrothermal system at Ehrenfriedersdorf, Germany: a SXRF study of melt and fluid inclusions

Received: 24 October 2005 / Accepted: 3 March 2006 / Published online: 22 April 2006

Abstract Detailed melt and fluid inclusion studies in quartz hosts from the Variscan Ehrenfriedersdorf complex revealed that ongoing fractional crystallization of the highly evolved H_2O-, B-, and F-rich granite magma produced a pegmatite melt, which started to separate into two immiscible phases at about 720°C, 100 MPa. With cooling and further chemical evolution, the immiscibilty field expanded. Two conjugate melts, a peraluminous one and a peralkaline one, coexisted down to temperatures of about 490°C. Additionally, high-salinity brine exsolved throughout the pegmatitic stage, along with low-density vapor. Towards lower temperatures, a hydrothermal system gradually developed. Boiling processes occurred between 450 and 400°C, increasing the salinities of hydrothermal fluids at this stage. Below, the late hydrothermal stage is dominated by low-salinity fluids. Using a combination of synchrotron radiation-induced X-ray fluorescence analysis and Raman spectroscopy, the concentration of trace elements (Mn, Fe, Zn, As, Sb, Rb, Cs, Sr, Zr, Nb, Ta, Ag, Sn, Ta, W, rare earth elements (REE), and Cu) was determined in 52 melt and 8 fluid inclusions that are representative of distinct stages from 720°C down to 380°C. Homogenization temperatures and water contents of both melt and fluid inclusions are used to estimate trapping temperatures, thus revealing the evolutionary stage during the process. Trace elements are partitioned in different proportions between the two pegmatite melts, high-salinity brines and exsolving vapors. Concentrations are strongly shifted by co ncomitant crystallization and precipitation of ore-forming minerals. For example, pegmatite melts at the initial stage (700°C) have about 1,600 ppm of Sn. Concentrations in both melts decrease towards lower temperatures due to the crystallization of cassiterite between 650 and 550°C. Tin is preferentially fractionated into the peralkaline melt by a factor of 2–3. While the last pegmatite melts are low in Sn (64 ppm at 500°C), early hydrothermal fluids become again enriched with about 800 ppm of Sn at the boiling stage. A sudden drop in late hydrothermal fluids (23 ppm of Sn at 370°C) results from precipitation of another cassiterite generation between 400 and 370°C. Zinc concentrations in peraluminous melts are low (some tens of parts per million) and are not correlated with temperature. In coexisting peralkaline melts and high-T brines, they are higher by a factor of 2–3. Zinc continuously increases in hydrothermal fluids (3,000 ppm at 400°C), where the precipitation of sphalerite starts. The main removal of Zn from the fluid system occurs at lower temperatures. Similarly, melt and fluid inclusion concentrations of many other trace elements directly reflect the crystallization and precipitation history of minerals at distinctive temperatures or temperature windows.

Keywords Synchrotron radiation XRF · Fluid inclusions · Melt inclusions · Ehrenfriedersdorf · Sn–W deposit · Germany

Editorial handling: R. Moritz

K. Rickers
Hamburger Synchrotronstrahlungslabor HASYLAB at
Deutsches Elektronen-Synchrotron DESY,
Notkestrasse 85,
22603 Hamburg, Germany

K. Rickers (✉) · R. Thomas · W. Heinrich
GeoForschungsZentrum Potsdam,
Division 4, Telegrafenberg,
14473 Potsdam, Germany
e-mail: karen.rickers@desy.de
Tel.: +49-40-89982930
Fax: +49-40-89982787

Introduction

Granite pegmatites and their hydrothermal derivatives are known for the enrichment of trace elements and the formation of rare minerals of economic interest. Over the past decade, our understanding of pegmatite-related ore-forming processes has been considerably extended by detailed studies of melt and associated fluid inclusions (e.g., Webster et al. 1997; Thomas et al. 2000, 2003, 2005; Thomas and Webster 2000; Audétat and Pettke 2003; Kamenetsky et al. 2004). Melt and fluid inclusions are

small blebs of silicate melt and aqueous fluids, respectively, which become included in host minerals during crystallization (e.g., Roedder 1984; Lowenstern 2003). They often provide the only direct information on the composition of phases present at mineral crystallization (Roedder 1984, 2003). During the evolution of granite–pegmatite–hydrothermal systems, single quartz hosts may continuously trap inclusions that record all stages of the chemical development of melts and fluids (cf. above). If correctly interpreted, melt and fluid inclusion suites give not only information about the evolution in time, but also about the effects that pressure and temperature changes have on melt and fluid compositions and concomitant crystallization sequences. This is particularly important at the pegmatite–hydrothermal transition because fractionation of many trace elements and enhanced partitioning into aqueous fluids occurs at this level.

The meaning of fluid and melt inclusions has been interpreted in a controversial way, due to the question of whether granitic pegmatites formed from a single homogeneous parental liquid (London 1999) or from a mixture of genetically related fluid phases (Roedder 1992). According to the formation model, inclusions were either interpreted as remnants of the original melt due to boundary layer effects (London 1992, 1999) or as products of immiscibility processes. Experimental studies on synthetic peraluminous granite doped with H_2O, B, P, and F confirm that aluminosilicate melt, hydrous fluid, and hydrosaline melt can stably coexist at 450–900°C and 1–2 kbar in bulk compositions similar to the ones of the here-studied system (Veksler et al. 2002b). Based on those experimental studies and on the findings on the Zinnwald granite–pegmatite system (Thomas et al. 2005), we interpret the phases observed in this study as products of immiscibility processes.

Detailed melt and fluid inclusions studies in quartz hosts for the Variscan Ehrenfriedersdorf and Zinnwald Complexes (Erzgebirge, Germany) revealed in both cases a direct genetic relationship between highly evolved Sn-bearing granites, pegmatites, and hydrothermal tin–tungsten mineralizations (Webster et al. 1997, 2004; Thomas and Webster 2000; Thomas et al. 2000, 2003, 2005). Melt inclusions in the granites show a gradual transition towards embryonic pegmatite melts, along with enrichment of water, B, F, P, Sn, Rb, and other incompatible elements. Further enrichment of volatiles and advancing differentiation induced phase separation into immiscible silicate melts at about 700°C (P≈100 MPa) and water concentrations of 20 to 25 wt.%. Two conjugate melts developed during cooling: a water-poor (type-A) and a water-rich (type-B) melt. The solvus opens with decreasing temperature (Fig. 1), and crystallization of pegmatite melts was completed at about 500°C. This particular behavior is mainly due to the very high concentrations of B and F (plus P in the Ehrenfriedersdorf case) of up to several weight percents each, acquired by both pegmatite melts during ongoing evolution. Fluid saturation early in the magmatic system produced an additional fluid phase that coexisted with the pegmatite melts over the entire T-range of 700 down to 500°C, which is recorded in primary fluid inclusions trapped together with type-A and type-B melt inclusions. Towards lower temperatures, fluid inclusions within the same quartz hosts indicate the transition into a hydrothermal system within both complexes. The solvus of pegmatite melts of Zinnwald is somewhat more open than that of Ehrenfriedersdorf (Fig. 1), probably because in the former, F dominates over B and P, whereas in the latter, B and P prevail. The composition of both silicate melts in terms of most major elements is well known, even though there may be problems with the analysis of B-rich type-B inclusions that have been trapped near the solvus crest (Thomas et al. 2000, 2003). Several trace elements (Rb, Cs, Sn) within melt and fluid inclusions have been used to outline the evolution of Zinnwald magmatic–hydrothermal system (Thomas et al. 2005), whereas, up to now, a systematic trace element database for the Ehrenfriedersdorf system is still lacking.

The aim of this paper is to outline the behavior of trace elements during the evolution and cooling of the Ehrenfriedersdorf pegmatite–hydrothermal system by synchrotron radiation-induced X-ray fluorescence (SXRF) analysis of well-characterized melt and fluid inclusions. We will use homogenization temperatures and water contents of type-A and type-B melt inclusions to estimate the trapping temperatures, i.e., their position on the solvus boundaries shown in Fig. 1. Similarly, homogenization temperatures of fluid inclusions will reveal the evolutionary stage of trace element-bearing fluids during the process. We will show that some trace element distributions outline the solvus for both pegmatite melts given in Fig. 1, and that melt and fluid inclusion compositions give information as to at which stages Sn and Zn mineralization occurred. We further show the usefulness of the SXRF method for detecting and

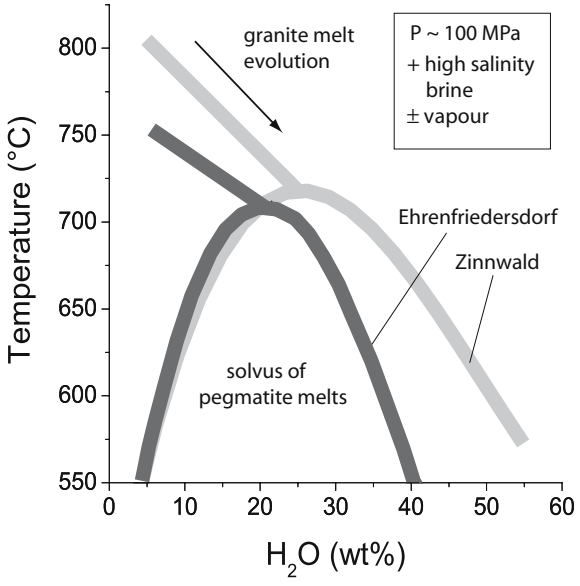

Fig. 1 Schematic pseudobinary plot of temperature vs water concentration depicting the solvus of two coexisting pegmatite melts at the Ehrenfriedersdorf and Zinnwald deposits. High-salinity brines and water-rich vapor are present during several stages of the pegmatite evolution (adapted from Thomas et al. 2000, 2003, 2005)

identifying very small daughter crystals within fluid inclusions, and we will also demonstrate that Raman spectroscopy may provide a wealth of information about suites of daughter crystals which are particularly abundant in volatile-rich type-B melt inclusions.

Geological setting and sample characteristics

The evolution of the granite–pegmatite–hydrothermal system of Ehrenfriedersdorf has been documented previously (Webster et al. 1997; Thomas and Webster 2000; Thomas et al. 2000, 2003). The work mainly focused on melt and fluid inclusion compositions in terms of major elements and their changes with temperature. The results are briefly summarized here. The Variscan granites are high-F, high-P, Li-mica granites rich in accessories such as zircon, monazite, xenotime, and uraninite (Förster et al. 1999). These granites crystallized at a lithostatic pressure of about 100 MPa, close to the surface. The related pegmatites are typically composed of quartz, orthoclase, albite, muscovite, and Li-bearing micas, with minor amounts of topaz, cassiterite, beryl, fluorapatite, and tourmaline. The pegmatite body is in endocontact with the Sauberg granite and has a size of about 200 m^3. Numerous melt and fluid inclusions are preserved in pegmatite quartz, and detailed petrographical observations allow for establishing a temporal sequence of their entrapment. Pegmatite quartz crystals continuously trapped two different types of melt inclusions during cooling and growth: a silicate-rich, relatively water-poor melt (type-A) and a silicate-poor, water-rich melt (type-B). Both melts were trapped on the solvus boundaries of the silicate (+ fluorine + boron + phosphorus)–water system (Fig. 1). This peculiar behavior results from the fact that F, B, and P amount to major elements when the pegmatite stage is attained after crystallization of the main granite body. The critical point of the system is at about 710°C at 100 MPa and about 20 wt.% H_2O. During cooling, the water content of type-A melts is reduced, that of type-B melts enriched, and the last pegmatite melts are trapped at 490°C, where type-A melts have about 3 wt.% of water, and type-B melts, about 45 wt.% of water. Boron is preferentially enriched in type-B melts (4 wt.% in B-melt vs 3 wt.% in A-melt at 650°C). Phosphorus and fluorine with absolute concentrations of several weight percents show similar behavior. The striking point is that the presence of these elements in major amounts dramatically decreases the critical pressure of fluid–melt systems. In addition, the same quartz crystals contain primary and secondary fluid inclusions. Hypersaline, high-temperature fluid inclusions were trapped from 680 to 550°C, indicating that cogenetic brines coexisted throughout the pegmatite-forming history. Towards lower temperatures, a hydrothermal system developed, which is recorded by fluid inclusions of lower salinities trapped between 500 and 370°C. The hydrothermal system changed from closed to open system behavior at about 440°C, where boiling processes occurred. Boron plays an important role in the whole process. Thus, Thomas et al. (2003) used boron concentrations in all fluid and melt phases at all stages to trace the complex evolution of the Ehrenfriedersdorf granite–pegmatite–hydrothermal system.

The analysis of major elements in melt inclusions is not trivial. At room temperature, both types consist of liquid, vapor, and a large variety of daughter crystals (Fig. 2a,b). Both melt inclusion types are mostly isometric with diameters of 20 to 80 μm. Some very large B-melt inclusions have diameters up to 200 μm. The major distinctive feature is their variable liquid to solid and vapor to solid ratios. Type-A melt inclusions have a low liquid to solid ratio (Fig. 2a), which decreases from early to late growth zones. Type-B melt inclusions have high liquid to solid and high vapor to liquid ratios (Fig. 2b), which further increase from early to late growth zones reflecting increasing contents of water and other volatiles. For analysis, inclusions must be rehomogenized under pressure to prevent decrepitation, followed by rapid quenching. For type-A melts, this produces homogeneous glasses (Fig. 2c) that can be easily measured for major and minor elements by electron microprobe, secondary ion mass spectrometry, and Raman spectroscopic methods (cf. above). Type-B melts, due to their higher contents of water and other volatiles, are often unquenchable and exsolve into glass, liquid, and vapor during quenching (Fig. 2d). Glass and liquid must then be analyzed separately. This produces relatively large errors because fluid/glass volume ratios can only be estimated by visual inspection, and because some elements in the fluid phase, particularly alkalis, cannot be measured directly. Estimations of alkali concentrations in the liquid phase of type-B melts are therefore obtained by microthermometric measurements. Major element compositions of type-A melts and best estimates of B-melt compositions obtained from a large number of inclusions are given in Thomas et al. (2000, 2003). The essential point is that type-A melts are peraluminous, whereas type-B melts are mildly to strongly peralkaline (Thomas et al. 2000, their Table 2; Thomas et al. 2003, their Table 1). Another striking feature is that type-B melts at room temperature are undersaturated in SiO_2, despite the fact that they are entrapped in quartz hosts. This appears to be bizarre; however, rehomogenization of B-melt inclusions is always accompanied by a volume increase of the inclusion by 25 vol% in average (determined for 20 melt inclusions), produced by the uptake of SiO_2 from the quartz host into the melt (now glass) during rehomogenization (Fig. 2e,f). Undersaturated melt, not in equilibrium with quartz at room temperature, reacts with quartz host towards SiO_2-saturated equilibrium compositions during heating to the homogenization temperature. Further evidence of SiO_2 undersaturation is given by the presence of nepheline crystals rimmed by K-feldspar within the body of the quartz pegmatite (Thomas et al. 2003, their Fig. 3) and by tiny nepheline crystals within B-melt inclusions. Nepheline probably crystallized directly from type-B melts. The mechanism for the formation of peralkaline, SiO_2-undersaturated melts within a peraluminous granite–pegmatite system is presented in an accompanying paper (Thomas et al. in press). For our purpose here, it is important to note that SiO_2-concentrations of type-B melts given by

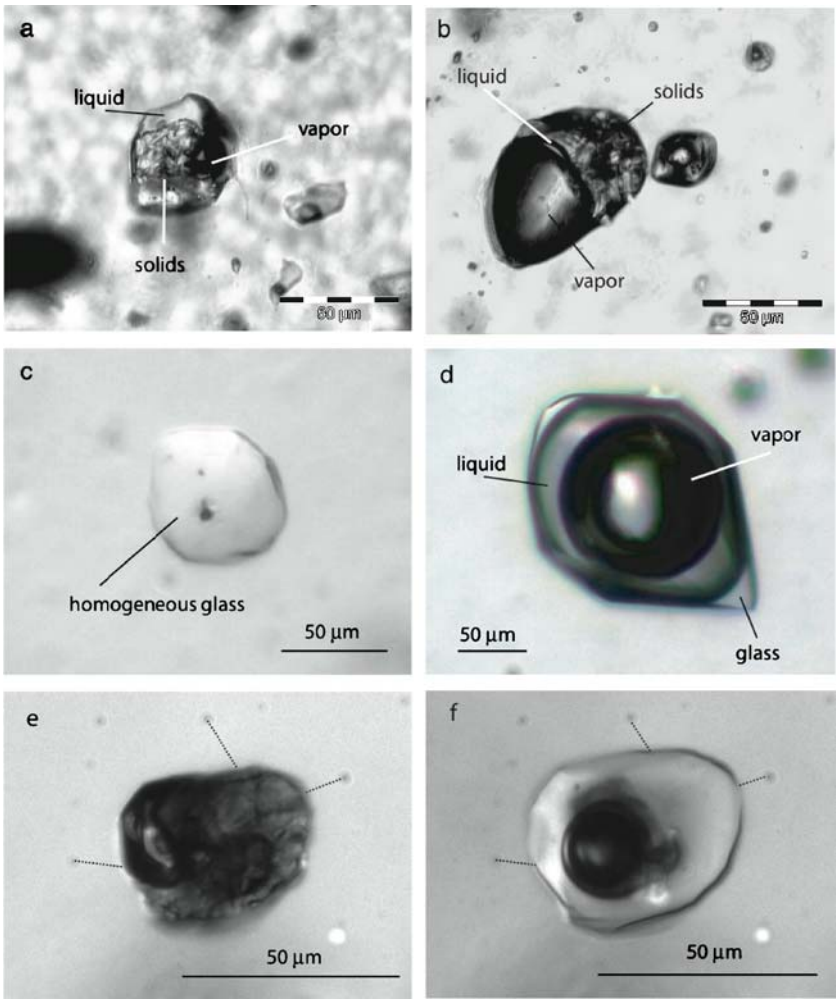

Fig. 2 Microphotographs of silicate melt inclusions in quartz hosts from Ehrenfriedersdorf. **a** Nonrehomogenized type-A melt inclusion containing liquid, vapor, and a large number of daughter crystals. **b** Nonrehomogenized type-B inclusion. **c** Rehomogenized type-A inclusion consisting of a homogeneous glass. **d** Type-B inclusion rehomogenized at 650°C. The originally homogeneous melt separated into glass, liquid, and vapor during quenching. **e** Type-B inclusion, nonrehomogenized. **f** Same inclusion, rehomogenized at 700°C. Note the volume increase by about 25% of the inclusion when rehomogenization is completed (*dashes*)

Thomas et al. (2000, 2003) are probably too high because analytical results of rehomogenized type-B melts did not account for uptake of SiO_2 from the host, and that measured trace element concentrations of rehomogenized type-B melts must be corrected for this effect. For SXRF, the analysis of heterogeneous melt (and fluid inclusions) is more straightforward: the difficulty of analyzing heterogeneous inclusions is overcome by measuring the complete inclusion either by using a broad beam or by performing area scans, thus establishing the comparability to the data obtained from single-point measurements of homogeneous inclusions.

Hypersaline fluid inclusions of the pegmatitic stage were simultaneously trapped with both melt inclusion types. They homogenize into the liquid phase between 680°C and 570°C. At room temperature, they contain a large variety of daughter crystals, including halite and sylvite. Total salinities are in the range of 30 to >50 wt.%, and NaCl/NaCl+KCl weight fractions are around 0.5. Varying amounts and sizes of silicate, phosphate, and fluorine- and boron-bearing daughter crystals do not allow for a "good" estimate of major element concentrations in these brines. Vapor-rich low-density fluid inclusions were also trapped during the pegmatitic stage. They homogenize into the vapor phase with apparent homogenization temperatures of ≥500°C, suggesting trapping temperatures of 700 to 500°C. From textural relationships between the four phases (A-melt, B-melt, hypersaline fluid, and vapor-rich fluid), it is unclear if they actually coexisted along the entire temperature range from 700 to about 500°C. Nevertheless, phase relations in a complex multicomponent system would permit the coexistence of two melts together with hypersaline brine and vapor. A reasonable scenario is that hypersaline brine continuously unmixed from the melt-dominated system at the early stage from the onset of melt–melt immiscibility down to 500°C, and that pressure fluctuations as commonly occurring near the roof of shallow intrusions induced the exsolution of vapor during events of pressure drop (for detailed discussion, see Thomas et al. 2003).

Trapping of type-A and type-B melts occurred down to 490°C. Below this temperature, the melt-dominated system changed to a fluid-dominated hydrothermal system recorded by abundant fluid inclusion suites. The vast majority homogenized between 480 and 360°C, and many of them show critical or near-critical homogenization with contrasting homogenization behavior in a narrow temperature range. A detailed description of the fluid

inclusions, including extensive microthermometrical data and an interpretation of the P–T–X evolution of the hydrothermal system, is given by Thomas (1982) and Thomas et al. (2003). For our purpose here, it is important that fluid inclusions representative of the early hydrothermal stage trapped at medium temperature (480 to 430°C) have intermediate salinities and a variety of transparent daughter crystals at room temperature, and that some contain brownish sphalerite crystals (Fig. 3a,b). The evolution towards later stages is transient, accompanied by intense boiling processes around 400°C. Consequently, salinities of liquids are highly variable at this stage, and vapor-rich inclusions are abundant (Thomas 1982). Concentrations of some distinctive trace elements in the three different types of fluid inclusions (pegmatite brines, early hydrothermal fluids, and later hydrothermal fluids) were previously published by Rickers et al. (2004). Here, we concentrate on the behavior of important trace elements, from the onset of the generation of pegmatite melts down to the late hydrothermal stage.

Experimental and analytical methods

Homogenization experiments of melt inclusions

Eight type-A and three type-B melt inclusions, which were proven to be suitable for the volatile loss-free homogenization of water-rich silicate melts, were selected (Webster et al. 2004) and experimentally rehomogenized using standard cold-seal pressure vessels. If possible, large, isometric, and undisturbed inclusions were used. The affiliation to the respective inclusion type should be recognizable. Small, polished chips 1 mm in thickness were loaded into an open Au capsule (30 mm long, 5 mm in diameter) and placed into a horizontal vessel. The vessel was pressurized with CO_2 to 1,000 bars, and then moved into the preheated furnace. Run temperatures were 700°C with a 50-h run duration. Pressure was manually controlled at 1,000 bars even during fast heating. Subsequently, the vessel was quickly removed from the furnace and quenched with compressed air. After quenching, the samples were removed, repolished to a thickness between 100 and 300 μm, and then used for SXRF analysis and for the determination of H_2O by confocal micro-Raman spectroscopy (Fig. 1c,d). For Raman analysis, the quartz samples were mounted on glass chips. All type-A melt inclusions were completely homogenized and consisted of a homogeneous glass. After the experiment, type-B inclusions consisted of glass + liquid + vapor that formed from a homogeneous water-rich melt during quenching (see Thomas et al. 2000, 2003, 2005, for detailed discussions).

Confocal laser Raman spectroscopy

The concentration of water in unopened type-A homogenized melt inclusions was determined by confocal Raman spectroscopy using a Dilor XY Laser Raman Triple 800-mm spectrometer, equipped with an Olympus optical microscope and a long-working-distance 80× objective. The 488-nm line of a Coherent Ar^+ Laser Model Innova 70-3 and a power of 450 mW of the argon laser were used for sample excitation, and spectra were collected with a Peltier cooled charge coupled device detector. Each spectrum was collected ten times, with a counting time of 50 s for each accumulation. The applied confocal pinhole size was 150 μm in diameter. Water concentrations were measured following the procedure described by Thomas (2000, 2002) and Thomas et al. (2000), which uses the ratio of the integral intensity of the asymmetric O–H stretching band between 3,100 and 3,750 cm^{-1}, and the asymmetric broad band in the 490-cm^{-1} region. Water concentrations of the glassy part of unmixed type-B inclusions were determined similarly. The total amount of water in type-B melt inclusions is the sum of water dissolved in glass plus that of the exsolved aqueous liquid. The latter was estimated using the microthermometric–volumetric method of Naumov (1979). For details, see Thomas et al. (2000, 2003).

Confocal laser Raman spectroscopy was also applied for the identification of the suites of daughter crystals other than halite and sylvite that are present in melt and fluid inclusions. To reduce the light absorption, the sample plates were polished on both sides in such a way that only a very thin layer was left on the two sides above and below the investigated inclusion (~10 μm). The diagnostic Raman bands for the most important daughter phases are given in Table 1. The position of the Raman band was controlled using the principal plasma lines in the Argon laser.

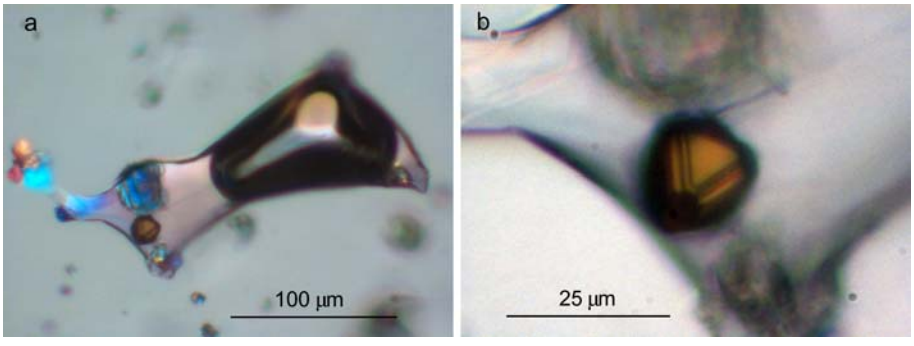

Fig. 3 **a** Microphotograph of a fluid inclusion in quartz host from Ehrenfriedersdorf pertaining to the later hydrothermal stage of the deposit. Daughter crystals are several phosphates, borates, and carbonates, along with a sphalerite crystal. **b** Blow-up of **a**, showing the brownish FeS-rich sphalerite

Table 1 Daughter minerals in different melt and fluid inclusion types of pegmatite quartz from Ehrenfriedersdorf

Mineral[a]	Characteristic Raman bands (cm^{-1})	Melt inclusions		Fluid inclusions		
		Type-A	Type-B	High-T	Medium-T	Low-T
Orthoclase $KAlSi_3O_8$	512.8	X	X			
Albite $NaAlSi_3O_8$	475.0, 502.8	X				
Nepheline $NaAlSiO_4$	399, 415, 920, 967		X			
Muscovite $KAl_2(Si_3Al)O_{10}(OH,\mathbf{F})_2$	192.0, 260.1, 408.9, 636.2, 700.4 (triplet)	X	(X)[b]			
Topaz $Al_2SiO_4(\mathbf{F},OH)_2$	238.0, 266.0, 285.0 (triplet)	X	X	X		
Boromuscovite $KAl_2(Si_3\mathbf{B})O_{10}(OH,\mathbf{F})_2$	555, 717, 3,614		X	X	X	
Diopside $CaMgSi_2O_6$	391, 666, 1,012		X			
Berlinite $Al\mathbf{P}O_4$	1,110.9	X	(X)[b]			
Fluorapatite $Ca_5(\mathbf{P}O_4)_3\mathbf{F}$	962.0	X				
Amblygonite $LiAl(\mathbf{P}O_4)(\mathbf{F},OH)$	601.0, 644.0, 1,011.2		X	X		
Lacroixite $NaAl(\mathbf{P}O_4)\mathbf{F}$	608.6, 622.7, 1,000.8	X	X	X		
Herderite $Ca\mathbf{Be}(\mathbf{P}O_4)\mathbf{F}$	584, 595, 983, 1,005		X	X		
Triplite $(\mathbf{Mn},\mathbf{Fe},\mathbf{Mg},\mathbf{Ca})_2(\mathbf{P}O_4)(\mathbf{F},OH)$	980.2					
Halite NaCl	–		X	X	X	X
Sylvite KCl	–		X	X		
$\mathbf{Li}_2CO_3$	1,090.8		(X)	X		
Calcite $CaCO_3$	1,085.0		X	X	X	(X)
Cryolite $Na_3Al\mathbf{F}_6$	552			X		
Elpasolite $K_2NaAl\mathbf{F}_6$	325.7, 558.5		X			
Sassolite $H_3\mathbf{B}O_3$	500, 880		X	X	(X)	
Ca–Mg–hexaborates $Mg\mathbf{B}_6O_{10}$, CaB_6O_{10} with 4 to 7.5 H_2O	634, 638, 641, 852, 855, 861, 953, 964		X	X		
Alkali tetrafluoroborate $M\mathbf{B}F_4$[c]	772		X			
Lithiummetaborate $\mathbf{LiB}O_2$	713, 1,459		X			
Cassiterite $\mathbf{Sn}O_2$	632.8	X	X			
Sphalerite **ZnS**	348.8			(X)	X	
Huebnerite $\mathbf{Mn}(\mathbf{W}O_4)$	881		X		X	
W–Nb-tantalites (wolframoixiolite) $(Fe,Mn,\mathbf{Nb})(\mathbf{Nb},\mathbf{W},\mathbf{Ta})O_4$	395, 526, 868		X			
Hematite Fe_2O_3	225, 245, 291				X	

Phases are determined by optical microscopy, Raman spectroscopy, and electron microprobe. Symbols in parentheses denote trace amounts of the respective daughter minerals

[a]The main mineral phases (quartz, orthoclase, albite, topaz, lacroixite) in A and B melt inclusions have identical compositions; only the phase proportions are different

[b]Formation after rehomogenization and cooling

[c]M=Na, K, Rb, Cs

Estimation of bulk compositions and water concentrations by optical microscopy

The composition of some nonrehomogenized type-B melt inclusions was estimated by determining the volume ratios of daughter crystals, liquid, and vapor. Large (up to 200 μm in diameter) and geometrically well shaped inclusions were used for estimation. The errors in volume estimation by normal optical observation are in the order of ±20% or better (Naumov 1979; Diamond 2001). This error was reduced to about ±10% by three-dimensional survey of the inclusions using a modified spindle stage equipped with a micrometer ocular (Anderson and Bodnar 1993). From the estimated volumes and the compositions and densities (given in the *Handbook of Mineralogy*, Vol. I–VI) of each mineral phase, the element concentrations in the melt inclusions were calculated. A problem is the correct estimation of the SiO_2 concentrations due to various degrees of reaction of the melt with the quartz host (see discussion in the text, and Table 2). Water contents in nonrehomogenized type-A and type-B melts were estimated were estimated using the microvolumetric/microthermometric method of Naumov (1979). The comparison of rehomogenized (where water contents have been measured) and nonrehomogenized melt inclusions shows that the liquid to vapor ratios in type-A inclusions give a good approximation for the total water in the inclusions.

Microthermometry of aqueous fluid inclusions

Microthermometric measurements were performed using a calibrated LINKAM THMS 600 heating and freezing stage, together with a TMS92 temperature programmer and

Table 2 Chemical compositions of type-B melt inclusions, trapped near the solvus crest at 650±50°C, estimated from the daughter crystal and liquid volumes in very large inclusions (up to 200 μm in diameter) and SXRF analyses

	1 (wt.%)	2 (wt.%)	3 (wt.%)	Daughter mineral phases
SiO_2	16.9	30.8	24.3	Orthoclase, topaz
B_2O_3	4.7	4.0	4.1	Meyerhofferite, H_3BO_3
Al_2O_3	16.6	13.8	11.1	Orthoclase, topaz, amblygonite, lacroixite, elpasolite
FeO[a]	0.2	0.1	3.7	Hematite
BeO	0.3	0.2	0.4	Herderite
CaO	0.8	0.7	0.8	Meyerhofferite, herderite
Li_2O	0.9	0.7	0.4	Amblygonite
Na_2O	6.0	5.0	5.9	Amblygonite, lacroixite, halite, elpasolite, (+ solution)
K_2O	6.1	5.1	7.5	Orthoclase, (+ solution)
Rb_2O[a]	0.5	0.4	0.2	
Cs_2O[a]	0.2	0.1	0.1	
F	6.2	5.2	5.8	Topaz, lacroixite, amblygonite, elpasolite, herderite
Cl	5.2	4.3	6.7	Halite, sylvite, (+ solution)
P_2O_5	6.9	5.7	6.7	Amblygonite, lacroixite, herderite
SnO_2	0.1	0.1	0.2	Cassiterite
H_2O	32.0	27.0	26.0	
Sum	103.6	103.2	103.9	
Sum[b]	99.8	100.0	99.9	
ASI	0.77	0.78±0.24[c]	0.53	

The mean standard deviation of determinations is 26.7% (SiO_2±5.0%). Column 1 shows the estimated composition, column 2, the same composition recalculated to equilibrium with host quartz (plus about 20 wt.% SiO_2; see text). Column 3 is from Thomas et al. (2003) determined from rehomogenized inclusions

ASI aluminum saturation index

[a]Determined by SXRF

[b]Sum corrected for F and Cl

[c]Standard deviation of the ASI results from the mean standard deviation of the element determinations (±26.7%)

a LNP2 cooling system mounted on an Olympus microscope. The stage was calibrated with synthetic fluid inclusions of known density, composition, and various melting points. Measurements were performed under argon. The standard deviation depends on absolute temperature and is always better than ±2.5°C for temperatures greater 100°C, and is ≤0.2°C for cryometric measurements at temperatures <20°C. Samples were 100–300-μm-thick, doubly polished quartz chips.

Synchrotron radiation-induced X-ray fluorescence analysis

Trace element analysis of homogenized and nonhomogenized melt and fluid inclusions was carried out by SXRF analysis, which has the advantage of being nondestructive when compared with laser ablation inductively coupled plasma mass spectrometry. Measurements were performed at the microfluorescence beamline L (Lechtenberg et al. 1996) at Hamburger Synchrotronstrahlungslabor at Deutsches Elektronen-Synchrotron. The synchrotron radiation originated by deflection of a 4.5-GeV positron beam at a bending magnet with a radius of 12.12 m, yielding a white spectrum with a maximum flux at 16.6 keV and a usable spectral range from 2 to 80 keV. The highly brilliant synchrotron radiation with a broad spectral range enables the measurement of trace elements in buried samples, such as inclusions, and the simultaneous detection of trace elements with atomic numbers (Z) up to 82 via K-shell excitation. The simultaneous detection of heavy elements and the penetrative nature of the synchrotron beam allowing the measurement of deep inclusions are important advantages of SXRF over particle-induced X-ray emission, which is also frequently used for inclusion analysis (e.g., Kamenetsky et al. 2002). The characteristics of the set-up of beamline L in the white beam mode were described previously (Rickers et al. 2004). The positron beam current during measurements was between 60 and 150 mA. Applied absorbers were either a 0.2-mm-thick Cu foil or a 12-mm-thick Al foil. Most measurements of single inclusions were performed using W plate cross-slit systems only for collimation of the beam to 50×50 μm^2, or, in the case of analysis of smaller inclusions, to 40×40 μm^2. The optimum measurement position was found by line scans in the horizontal plane across the inclusion. The inclusion was measured at the position with the maximum fluorescence signal by single-point measurements, with sampling between 1,200 and 1,800 s. When elemental distributions of trace elements within single inclusions were measured, a glass monocapillary suitable for the collimation of hard X-rays was used, yielding a Gaussian-shaped beam with a full width half maximum (FWHM) of 12 μm in diameter impinging on the sample. Step sizes for line and area scan measurements were generally half the beam size, resulting in an improved spatial resolution. Due to the Gaussian

shape of the incident beam, the orientation of the sample at 45° to the indicent beam and the detector, and the position of the inclusion below the sample surface, it is difficult to precisely align the inclusion in the beam. To ensure that the scanned area completely covers the inclusion, a distance typically larger than the inclusion by a factor of 3–4 in the horizontal direction and by a factor of 2–2.5 in the vertical direction was scanned.

Sample times for area and line scan measurements varied between 15 and 60 s per point. An energy dispersive Ge detector with an energy resolution of 160 eV at 5.9 keV, in combination with a digital signal processor, was used for spectra acquisition.

For some selected inclusions, area scan measurements with the best spatial resolution available at beamline L were performed to detect the elemental compositions of small daughter crystals and/or vapor bubbles. To avoid misinterpretations on the potential of SXRF, it should be stated in this context that better spatial resolutions than the one used here are possible. The smallest reported beam sizes are below 1 μm FWHM. However, the optical tools generating such small beam sizes are mostly restricted to lower energies than the desired one. The measurements were performed using a single bounce capillary, which focuses the synchrotron beam to a spot size of 10 μm FWHM. This optical tool is restricted to energies below 40 keV, so that an excitation spectrum with maximum energies of 40 keV was applied using a double-crystal multilayer monochromator at 40 keV (Falkenberg and Rickers 2002). In case of monochromatic excitation, a Si (Li) solid state detector was used instead of the Ge detector, due to the frequent occurrence of escape peaks of the latter that overlap with the peaks of the elements of interest.

The quantification of the single-point measurements in the polychromatic mode was achieved in the standardless mode according to the procedure described by Rickers et al. (2004). Results were tested for accuracy and precision in two steps (e.g., Rickers et al. 2004): (1) area scans of synthetic glass standards yielded an accuracy of generally better than 20% for all elements with Z between 37 and 92. The standard deviation of the area scan measurements was better than 7%, whereas the repeatability of single-point measurements was better than 0.5%. (2) Single-point measurements of synthetic inclusions in quartz yielded an accuracy of better than 20% for concentrations well above the lower limit of detection (test elements: Rb and Cs), and still better than 30% for concentrations close to the lower limit of detection (test elements: Sn and Cu), with a lower reproducibility of 20% and a repeatability of 6% tested on one big Cu-bearing fluid inclusion (Rickers et al. 2004).

For the area scan measurements of fluid and melt inclusions, an accumulated spectrum of each scan was generated by summing up the normalized (to live time and positron beam current) spectra, which was fitted using the AXIL software (van Espen et al. 1992; Vekemans et al. 1995, 2004). The Cs peak area of the accumulated spectrum was then used to determine the Cs concentration within the inclusion by comparison to normalized peak areas of standard reference materials [National Institute of Standards & Technology (NIST) 612 and NIST 610] measured under the same experimental conditions, and by taking into account the different densities and the relations between inclusion and area scan volume. This Cs concentration was then used as an internal standard for quantifications using Monte Carlo simulations (Vincze et al. 1993, 1995a–c), as described by Rickers et al. (2004). Cesium was chosen as an internal standard because it was always present in the here-analyzed inclusions, and its concentration in these inclusions may be determined with a sufficient accuracy by external standardization without absorption corrections, due to the high energy of the fluorescence radiation absorbed by less than 5% in the covering quartz matrix.

Results and discussion

Daughter minerals

Table 1 shows the large variety of daughter minerals in type-A and type-B melt inclusions, and in fluid inclusions of the pegmatitic (high-T), early hydrothermal (medium-T), and late hydrothermal (low-T) stages present at ambient temperature that were detected by Raman spectroscopy, along with the characteristic Raman bands of each respective mineral. Peraluminous type-A melts crystallized the silicates orthoclase, albite, muscovite, and topaz, together with the phosphates berlinite, fluorapatite, and lacroxite. Sometimes, tiny cassiterite crystals were also present. Water-rich peralkaline B-melt inclusions crystallized up to 20 different mineral species, including halite; sylvite; silicates; nepheline; various phosphates and fluorophosphates; fluorides such as cryolite and elpasoite, borates, metaborates, carbonates, alkali tetrafluoroborates, cassiterite, huebnerite; and others (Table 1). These daughter minerals reflect the very high concentrations of alkalis and the volatiles B, P, and F, along with low Al and Si concentrations in the original melts. Their viscosities were very low, in the range of 1 Pa s (Veksler et al. 2002a), which explains the fact that rehomogenized melt inclusions of this type separate into silicate melt, liquid, and vapor, even during rapid quenching. High-temperature brine inclusions of the pegmatitic stage contain only topaz and boromuscovite as silicate phases; however, borates, fluorides, carbonates, and fluorophosphates are again present. Cassiterite is absent. Medium temperature inclusions from the early hydrothermal stage have much fewer daughter minerals. Boromuscovite is the only silicate phase, which occurs along with halite, calcite, and sassolite. Importantly, sphalerite and huebnerite are present in most of these inclusions. Late-stage hydrothermal fluid inclusions may contain halite and, in rare cases, calcite. Other daughters are absent.

Estimated composition of type-B melts via daughter crystals in type-B inclusions

Inherent difficulties in determining the bulk compositions of type-B melt inclusions result from the fact that rehomogenized inclusions exsolve into glass, liquid, and vapor during quenching. Glass and liquid are analyzed separately, and the total composition is the weighted sum of the composition of the two phases. Large errors result because the concentration of alkalis and some important volatiles can only be estimated. Therefore, the bulk compositions of type-B inclusions given by Thomas et al. (2000, 2003) are the best estimations at present. Moreover, SiO_2-concentrations estimated from rehomogenized (and subsequently exsolved) inclusions may be overestimated, because originally SiO_2-undersaturated melts may have acquired SiO_2 from the quartz host during rehomogenization. Another approach is to estimate the bulk composition by carefully determining the volume ratios of daughter crystals (previously identified by Raman spectroscopy, Table 1), liquid, and vapor by optical microscopy, and calculating the bulk composition via the weighted sum of the individual phase compositions. The result for a type-B melt inclusion trapped near the solvus crest is shown in Table 2, where column 1 represents the calculated bulk composition. Column 2 shows the bulk composition (column 1) plus the addition of 20 wt% of SiO_2 to make the result comparable to previous compositions obtained by the rehomogenization method (column 3). If the concentrations of column 1 are adequately estimated and if rehomogenized inclusions acquired 20 wt% SiO_2 from the quartz host, concentrations of columns 2 and 3 should agree. Given the (large) errors inherent in both methods, the results agree reasonably well for most elements. Larger deviations exist for H_2O and SiO_2. The variability of the water contents may be explained by the fact that H_2O concentrations of type-B melts trapped near the solvus crest are highly sensitive to

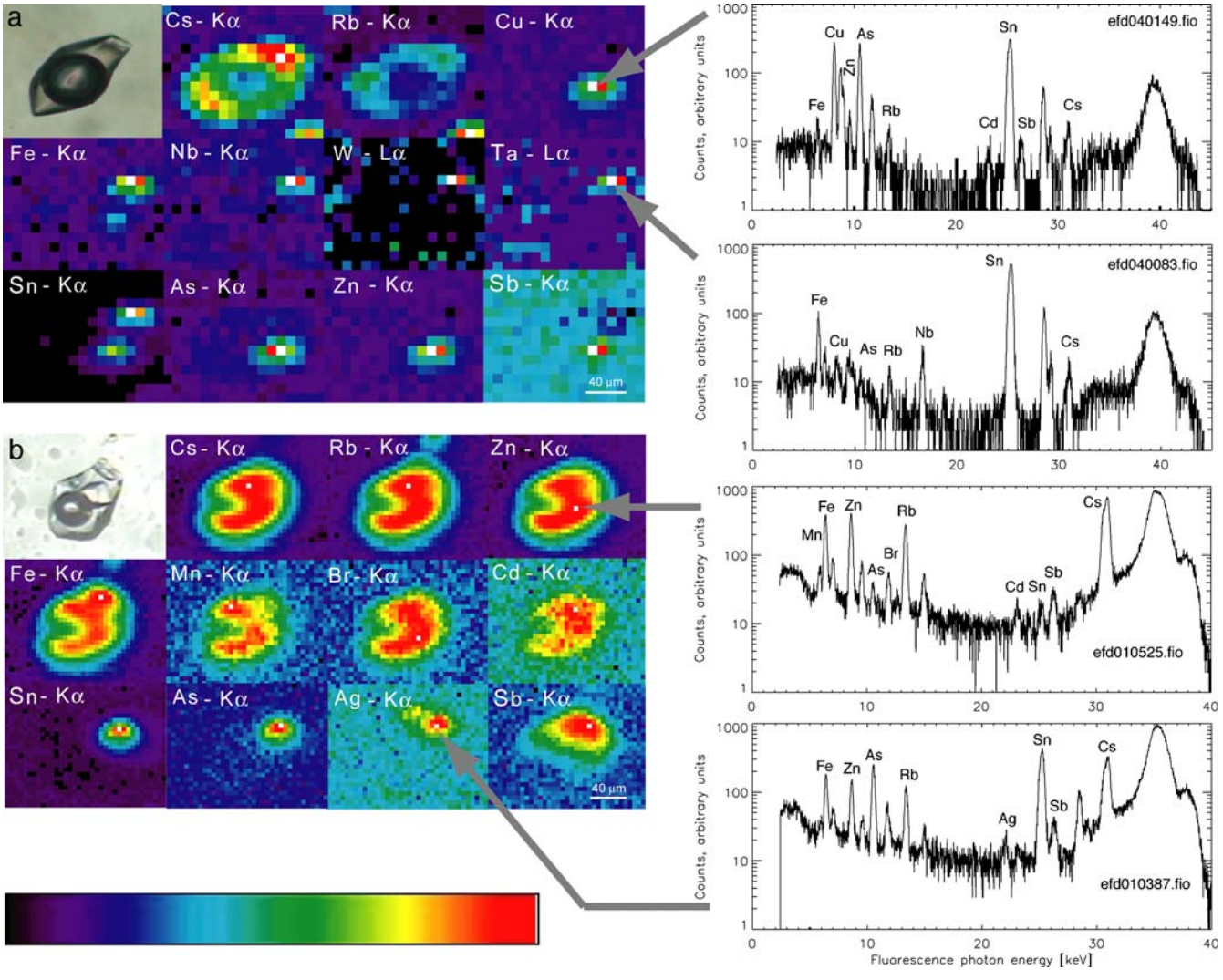

Fig. 4 Trace element distribution maps of fluid inclusions. **a** fluid inclusion (FI) from the early hydrothermal stage hosted in a quartz chip of 100 µm in thickness. Pixel size is 10×10 µm^2. **b** FI from the late hydrothermal stage hosted in a quartz chip of 300 µm in thickness. Pixel size is 5×5 µm^2. Relative intensity is given from 0 (*black*) to 1 (*white*) and not to scale. SXRF spectra at the right refer to analyses at spots indicated by *arrows*. For further explanation, see text

the trapping temperature (Fig. 1). Water concentrations increase from about 20 to 30 wt.% as temperature drops from 700 to 650°C, and our estimated trapping temperature for these particular inclusions is not better than ±50°C. Similar arguments hold for the variations in SiO_2, aside from the fact that we do not know to which extent the melt equilibrated with the host during homogenization. Trace element concentrations were measured in rehomogenized and in nonrehomogenized inclusions. Given the arguments above, we arbitrarily corrected the trace element concentrations for rehomogenized type-B melt inclusions for 25% uptake of SiO_2 from the quartz host.

Daughter crystals in fluid inclusions detected by SXRF area scans

Figure 4 shows distribution maps for selected trace elements of an apparently two-phase fluid inclusion from the early hydrothermal stage showing near-critical liquid–vapor homogenization (Fig. 4a), and of a hypersaline inclusion with halite and sylvite daughter crystals (Fig. 4b). In Fig. 4a, concentrations of the alkalis Rb and Cs depict the volume of the fluid phase in the inclusion projected onto the two-dimensional plane. The concentrations of all other elements in the fluid phase are very low, including those of Fe, Zn, and Sn. Step scans reveal that there are at least two, and probably more, minute crystals within the inclusion, which are invisible under the microscope. On the upper right-hand corner, there is clear indication of an Fe-, Nb-, W-, and Ta-rich mineral adhering at the inclusion wall, identified as wolframoixiolite $(Fe,Mn,Nb)(Nb,W,Ta)O_4$, which also occurs in B-melt inclusions. There is also a very strong Sn peak, indicative of cassiterite, as W–Nb-tantalites do not incorporate significant amounts of Sn. At the lower right-hand side, enrichments of As, Zn, Sb, and Cu suggest a complex (Sb,As,Ag,Cu)-sulfide, possibly argentotennantite or a similar mineral. Strong enrichment of Sn at this point (see Sn distribution at the lower left and SXRF spectrum above) probably reveals another cassiterite crystal. In Fig. 4b, concentrations of the alkalis again trace the volume of the fluid within the inclusion, as do Zn, Fe, Mn, Br, and Cd. Zinc and Fe concentrations in the salt-saturated fluid are much higher compared to those of the early hydrothermal stage. There are at least two additional invisible daughter crystals present: cassiterite and a (As, Ag,Sb)-rich phase, probably freibergite $(Ag,Cu,Fe)_{12}(Sb,As)_4S_{13}$, which is a mineral frequently observed in the Freiberg mining district. Both are located above or below the large halite crystal in the center of the inclusion (Fig. 4b).

These results confirm that for correct results, SXRF-spectra of the total inclusion volume are required. Apparently, two-phase L–V inclusions or L–V inclusions with salt crystals may contain minute invisible daughter crystals with trace elements that are important for understanding ore genesis. High spatial resolution allows for distinguishing whether important trace elements reside in fluids or whether they form distinctive mineral phases.

Trace element concentrations of melt and high-T fluid inclusions

Concentrations of 14 selected trace elements measured in 38 A-melt and 14 B-melt inclusions are presented in Table 3, along with their measured or estimated water contents and trapping temperatures. Table 4 shows concentrations of 13 trace elements in fluid inclusions, which are typical for the pegmatitic, early hydrothermal, and late hydrothermal stages, along with measured salinities and homogenization temperatures.

The alkalis Rb and Cs nicely trace the compositional evolution of type-A and type-B melts. Rubidium concentrations in type-A melts decrease from 5,400 to lower than 100 ppm in the temperature range from 700 to 500°C, and in type-B melts, from 5,800 to about 100 ppm. The plot of Rb vs water concentrations along with estimated isotherms roughly outlines the two boundaries of a pseudobinary solvus between the two immiscible melts (Fig. 5). Rubidium shows a slight preference for the water-rich type-B melts relative to type-A melts at all temperatures. Between 700 and 500°C, Rb concentrations decrease by more than one order of magnitude. Two major fractionation effects are responsible for this: (1) Concomitant crystallization of Rb-rich boromuscovite (1.24 wt.% Rb_2O; Thomas et al. 2003) and K-feldspar (2.38 wt.% Rb_2O; Thomas and Webster 2000) depletes both melts in Rb over the entire temperature range. Boron- and P-rich alkali feldspar with 2.1 wt.% Rb_2O and 7.9 wt.% Cs_2O has been found in the Ehrenfriedersdorf pegmatite body (Thomas, unpublished data). (2) Partitioning into coexisting brines (in the range of 1,000 ppm Rb; Table 4) that may continuously exsolve from the melts removes Rb during the cooling of the system. Cesium behaves very similarly and shows a good correlation with Rb (Fig. 6a). Concentrations range from 2,500 to lower than 100 ppm in type-A melts, and from 1,900 to lower than 100 ppm in type-B melts over the same T-range, due to similar effects of silicate crystallization and brine exsolution. The correlation is weaker at high concentrations of both, i.e., at high temperatures, probably reflecting compositional shifts near the crest of the solvus induced by small pressure–temperature fluctuations.

Because Rb is a good monitor of the compositional evolution of the pegmatite melts, concentrations of other trace elements vs Rb are shown in Fig. 6a–e. Concentrations of Sn roughly correlate with Rb (Fig. 6b) with 1,500 to about 50 ppm in type-A melts, and 1,500 to about 70 ppm in type-B melts from 700 to 500°C (Table 3). Data scatter, particularly at high temperatures between 650 and 700°C, but at lower temperatures, there is clear indication that Sn preferentially fractionates into type-B melts, roughly by a factor of 2 to 5 (see also Fig. 9, below). Previous investigations of Thomas and Webster (2000) revealed even higher Sn concentrations of up to 7,000 ppm Sn in some very rare A- and B-melt inclusions trapped at the initial stage of pegmatite melt formation. Decrease in Sn concentrations is due to crystallization of cassiterite throughout the pegmatitic stage. This is in line with earlier models on the genesis of the tin ores at Ehrenfriedersdorf

suggesting a two-stage formation of cassiterite, an early one at pegmatitic and a late one at hydrothermal conditions (e.g., Dahm and Thomas 1985; and below). High-temperature brines contain up to 400 ppm of Sn (Table 4).

Concentrations of the semivolatiles As and Sb also roughly correlate with that of Rb (Fig. 6c). Most As concentrations are between 1,000 and 500 ppm at high temperatures, and decrease down to values in the range of 100 ppm at low temperatures. Data scatter considerably, but indicate an overall preference of As into type-B melts (Table 3). Antimony behaves similar, with lower total concentrations of 40 to 50 ppm at high temperature, and a few parts per million at low temperature. There is no evidence of crystallization of As and Sb-bearing minerals during the pegmatitic stage at Ehrenfriedersdorf. A reasonable assumption is that depletion occurred by fractionation into exsolving fluids. High-temperature brines contain up to 170 ppm of As and 20 ppm of Sb (Table 4). High-temperature vapor-rich inclusions contain between 120 and 180 ppm of As (data from Rickers et al. 2004). Thus, vapor could have easily extracted the semivolatiles As and Sb from the melt system.

Of the group of high field strength elements, Nb shows a rough correlation with Rb. Concentrations range between 200 and 50 ppm at high temperatures, and a few parts per million at low temperatures in both melts (Fig. 6d). This is explained by concomitant crystallization of W–Nb-tantalites found in the pegmatite body, and also in some B-melt

Table 3 Trace element compositions, water contents, and estimated trapping temperatures for type-A and type-B melt inclusions

	Mn (ppm)	Fe (ppm)	Zn (ppm)	As (ppm)	Rb (ppm)	Sr (ppm)	Zr (ppm)	Nb (ppm)	Ag (ppm)	Sn (ppm)	Sb (ppm)	Cs (ppm)	Ta (ppm)	W (ppm)	H_2O (wt.%)	T (°C)
Type-A	31	1,132	27	1,047	4,990	b.d.	25	84	b.d.	628	27	1,294	521	145	25.0	700
melts	43	1,567	30	26	5,246	b.d.	20	131	b.d.	1,523	30	691	936	b.d.	25.0	700
	149	2,209	22	1,070	5,080	16	40	102	3	721	37	2,113	b.d.	202	20.2[a]	700
	549	2,816	43	1,007	5,436	17	87	86	3	629	28	1,612	b.d.	104	19.6[a]	700
	b.d.	2,671	25	1,399	4,011	27	39	96	15	1,336	47	1,489	b.d.	75	17.6[a]	>650
	21	781	14	616	4,108	b.d.	11	78	b.d.	435	21	914	701	97	16.0	>650
	b.d.	2,444	13	946	3,838	32	51	78	3	1,237	28	1,085	b.d.	64	14.7[a]	>650
	2,024	12,064	380	685	2,274	37	23	37	1	568	37	2,479	b.d.	23	26.2[a]	650
	1,044	3,710	17	496	3,333	25	b.d.	72	12	952	44	618	b.d.	97	23.6[a]	650[b]
	11	665	12	504	3,499	b.d.	1	28	b.d.	308	44	831	323	53	18.0	650[b]
	b.d.	12,735	b.d.	849	3,396	b.d.	b.d.	232	b.d.	1,217	b.d.	849	b.d.	b.d.	16.0	650
	b.d.	5,430	b.d.	815	3,258	b.d.	b.d.	145	b.d.	1,086	b.d.	778	b.d.	b.d.	15.0	650
	b.d.	70	13	145	1,772	b.d.	b.d.	1	b.d.	569	b.d.	1,144	464	b.d.	12.0	650
	b.d.	52	4	18	65	b.d.	b.d.	3	b.d.	23	11	77	179	b.d.	10.0	650
	b.d.	348	12	137	1,516	b.d.	b.d.	31	b.d.	472	25	370	1,033	b.d.	10.0	650
	b.d.	1,866	11	781	2,327	b.d.	26	91	3	635	32	596	b.d.	43	9.6[a]	650
	302	1,770	16	548	2,724	19	23	41	3	603	23	764	b.d.	68	14.1[a]	>600
	b.d.	15,100	b.d.	755	1,727	b.d.	b.d.	91	b.d.	453	b.d.	453	b.d.	b.d.	12.0	600
	b.d.	b.d.	b.d.	724	1,991	b.d.	b.d.	112	b.d.	362	b.d.	543	b.d.	b.d.	12.0	600
	5	248	12	1	1,921	b.d.	5	52	b.d.	90	22	416	426	72	10.0	600
	b.d.	801	36	345	1,708	b.d.	b.d.	22	b.d.	335	19	631	228	b.d.	10.0	600
	b.d.	3,557	20	14	1,008	b.d.	b.d.	5	b.d.	99	14	153	111	b.d.	10.0	600
	b.d.	9,060	b.d.	906	1,586	b.d.	b.d.	113	b.d.	340	b.d.	453	b.d.	b.d.	10.0	600
	b.d.	204	24	313	1,424	b.d.	b.d.	2	10	557	17	898	498	b.d.	10.0	600
	b.d.	75	5	159	1,088	b.d.	b.d.	4	2	219	13	518	196	b.d.	10.0	580
	b.d.	b.d.	b.d.	b.d.	906	b.d.	b.d.	63	b.d.	227	b.d.	151	b.d.	b.d.	8.0	580
	622	6,324	86	1,884	530	6	58	149	2	1,073	41	2,343	b.d.	101	16.0	550
	b.d.	489	24	233	1,151	b.d.	b.d.	19	b.d.	297	25	347	556	b.d.	15.0	550
	b.d.	293	18	147	1,001	b.d.	b.d.	12	b.d.	145	20	286	268	b.d.	12.0	550
	b.d.	302	30	231	854	b.d.	b.d.	22	b.d.	290	33	362	399	b.d.	12.0	550
	b.d.	409	24	9	1,102	b.d.	b.d.	30	b.d.	408	5	161	283	292	9.0	550
	b.d.	29	3	47	432	b.d.	b.d.	9	b.d.	92	4	212	b.d.	1	8.0	550
	19	774	6	7	122	b.d.	5	3	b.d.	39	7	47	35	b.d.	8.0	550
	b.d.	b.d.	b.d.	604	906	b.d.	b.d.	63	b.d.	302	b.d.	453	b.d.	b.d.	8.0	550
	b.d.	45	11	102	662	b.d.	b.d.	4	3	155	b.d.	325	674	b.d.	8.0	550
	b.d.	495	33	193	760	b.d.	b.d.	17	4	253	5	287	230	7	8.0	550
	b.d.	15	12	23	147	b.d.	b.d.	1	b.d.	48	b.d.	112	169	b.d.	6.0	550
	b.d.	37	9	26	14	b.d.	b.d.	b.d.	b.d.	64	4	18	16	b.d.	5.0	500

Table 3 (continued)

	Mn (ppm)	Fe (ppm)	Zn (ppm)	As (ppm)	Rb (ppm)	Sr (ppm)	Zr (ppm)	Nb (ppm)	Ag (ppm)	Sn (ppm)	Sb (ppm)	Cs (ppm)	Ta (ppm)	W (ppm)	H_2O (wt.%)	T (°C)
Type-B	289	8,123	125	1,796	5,775	b.d.	43	120	b.d.	1,492	33	1,306	751	b.d.	30.0	720
melts	25	1,104	32	3	5,739	b.d.	36	165	b.d.	1,287	36	1,255	1,180	b.d.	30.0	720
	b.d.	1,663	106	1,540	5,377	b.d.	b.d.	98	7	1,120	40	1,913	1,166	45	35.0	700
	27	828	32	720	4,328	b.d.	17	52	b.d.	530	37	902	703	186	40.0	650
	41	1,463	30	1,068	4,563	b.d.	27	97	b.d.	878	28	1,381	517	134	45.0	650
	b.d.	711	153	778	3,314	b.d.	b.d.	76	35	1,320	28	1,294	1,559	13	45.0	600
	511	3,151	84	1,045	2,740	b.d.	33	94	1	751	21	1,713	b.d.	85	47.4[a]	<600
	1,482	4,852	1	617	1,313	b.d.	b.d.	29	1	64	40	1,769	b.d.	38	30.0	550
	196	1,769	72	763	1,487	b.d.	18	33	9	653	39	790	b.d.	53	37.8[a]	550[b]
	b.d.	4,106	78	74	1,237	b.d.	5	17	b.d.	166	6	266	106	34	50.0	550[b]
	28	641	20	707	1,677	b.d.	4	30	b.d.	476	16	440	191	b.d.	50.0	550
	437	1,732	39	767	1,160	b.d.	29	28	2	843	10	481	b.d.	55	51.2[a]	550
	b.d.	410	15	89	1,317	b.d.	b.d.	21	b.d.	192	11	442	245	b.d.	50.0	550
	b.d.	48	8	41	143	b.d.	1	2	b.d.	68	3	44	66	b.d.	52.0	500

b.d. below the lower limit of detection
[a]Measured by Raman spectroscopy
[b]Indications of heterogeneneous trapping of type-A and type-B melts

inclusions (Table 1). Tantalum shows no systematic behavior. It attains maximum concentrations of 1,500 and 1,000 ppm in type-B and type-A melts, respectively, and is absent in others. Maximum concentrations are always below the level of columbite saturation, which is as high as 2,000 to 4,000 ppm of Ta in F- and Li-rich granitic melts at 600°C (Linnen 1998; Linnen and Keppler 1997), explaining the absence of columbite at Ehrenfriedersdorf. If detectable, Nb/Ta ratios are below 0.2 (Fig. 6e), indicating the extremely high fractionation degree of the melts. Very low Nb/Ta ratios already present in high-temperature melts trapped near the solvus crest confirm that the high fractionation degree was attained before the evolved parent-melt separated into two pegmatite melts at about 700°C. This holds also for the removal of Zr from the melt system. Zirconium concentrations attain notable amounts only in high-temperature type-A melts, with 11–87 ppm above 650°C. Zirconium is below detection limits at lower temperatures. In type-B melts, the maximum Zr concentration is 43 ppm (Table 3). In fluid inclusions, there is no Zr detectable.

In none of the melt and fluid inclusions could REE be detected. Detection limits for REE in comparable melt inclusions are in the range of tens of ppm (Rickers et al. 2004). Highly evolved granite melts often have light REE contents fairly above these lower limits of detection. Significantly lower contents in our melt inclusions indicate that REE fractionation occurred at an earlier evolutionary stage. This is supported by ubiquitous monazite, xenotime, and apatite in the Ehrenfriedersdorf granite and its early-stage derivatives (Thomas et al. in press). Strontium is below the lower limits of detection in all inclusions, except

Table 4 Trace element compositions, salinities, and homogenization temperatures of aqueous fluid inclusions representative for various stages of the hydrothermal evolution

Stage	Mn (ppm)	Fe (ppm)	Cu (ppm)	Zn (ppm)	As (ppm)	Rb (ppm)	Nb (ppm)	Ag (ppm)	Sn (ppm)	Sb (ppm)	Cs (ppm)	Ta (ppm)	W (ppm)	$NaCl_{equivalent}$ (wt.%)	Th (°C)
Pegmatitic															
1	b.d.	144	b.d.	28	173	986	10	29	404	21	569	n.d.	b.d.	52	681
2	b.d.	13	b.d.	99	11	13	b.d.	b.d.	25	12	15	n.d.	b.d.	40	640
3	b.d.	116	194	41	155	255	b.d.	b.d.	104	b.d.	245	n.d.	b.d.	32	550
Early hydrothermal															
4	b.d.	356	481	130	274	439	12	b.d.	350	37	263	n.d.	b.d.	31.4	484
5	b.d.	1,004	1,286	182	496	1,507	29	b.d.	855	171	342	n.d.	b.d.	15	440
Later hydrothermal															
6	583	2,442	23	737	173	231	b.d.	b.d.	36	50	530	n.d.	b.d.	5	400
7	1,842	7,844	115	2,980	291	824	b.d.	b.d.	113	127	1,973	n.d.	b.d.	50	400
8	1,058	3,102	59	1,297	37	254	b.d.	b.d.	23	57	656	n.d.	b.d.	10	380

Rows 1 and 2 are single fluid inclusions; rows 3 to 8 are average compositions of several fluid inclusions as reported by Rickers et al. (2004)
b.d. below the lower limit of detection, *n.d.* not determined

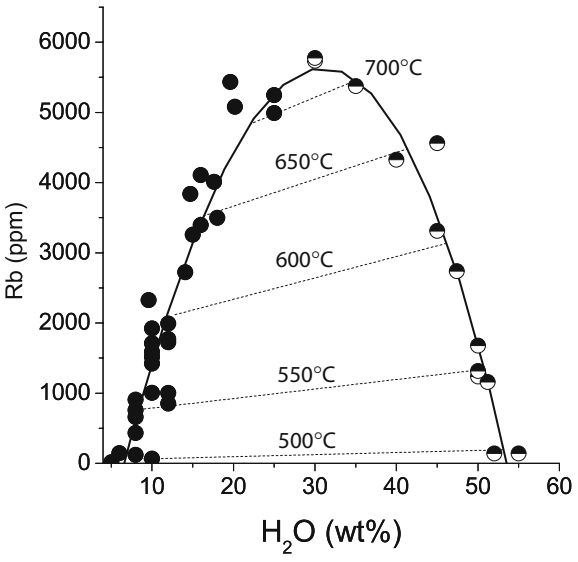

Fig. 5 Rubidium concentrations of type-A (*filled circles*) and type-B (*open circles*) melt inclusions trapped at different temperatures plotted vs their water concentrations, along with the respective isotherms. Rubidium concentrations trace the shape of the solvus and significantly decrease with decreasing temperatures in both melt types. Data are from Table 3

of some high-temperature type-A melts (17–37 ppm Sr). Similar to REE, Sr fractionated into Cl- and F-rich apatite present in the granite, but also into albite.

Tungsten concentrations are highly variable. Concentration ranges in type-A and type-B melts are similar with 1–292 ppm, and 13–186 ppm, respectively, and in many of them, W is below the lower limits of detection. There is no correlation of W with Sn contents in melt inclusions. Tungsten is absent in all fluid inclusions. Silver is mostly below the lower limits of detection in both types of melt inclusions. Maximum concentrations are 15 ppm in type-A and 35 ppm in type-B melts, and there is no systematic variation with temperature. Up to 29 ppm of Ag is present in high-temperature brines. There is no detectable Cu in melt inclusions and in brines of the pegmatitic stage that were trapped at 680°C and 640°C. In brines trapped at 550°C, Cu becomes enriched and amounts to about 200 ppm (Table 4).

The first series transition metals Fe and Mn display very large scatters in concentrations. Iron contents in melts range between 0 and 15,000 ppm, and those of Mn, between 0 and 2,000 ppm. The large scatter allows neither for distinguishable fractionations between the melt types nor for correlations with other trace elements. There is, however, a trend towards lower concentrations with decreasing temperature, particularly for Fe contents in type-A melts. Manganese concentrations in high-T brines are below the lower limits of detection, and those of Fe are low (about 100 ppm; Table 4). Zinc concentrations in melt inclusions are low. Type-A melts contain between a few and several tens of parts per million of Zn, not correlated with temperature (with one exception of 380 ppm). Zinc concentrations of type-B melts are systematically higher by a factor of 2 to 3, attaining values of up to about 150 ppm (see inset of Fig. 10, below), indicating preference of Zn into type-B melts. High-temperature brines contain similar amounts of Zn, up to about 100 ppm (Table 4).

Alkali elements, tin, copper, and zinc, from the early pegmatitic to the late hydrothermal stage

In previous contributions by Thomas et al. (2000, 2003) have argued that, at Ehrenfriedersdorf, the compositional evolution of melts and fluids from the early pegmatite to the late hydrothermal state is mostly gradual, as indicated, for example, by the boric acid concentration in melt and fluid inclusions (Thomas et al. 2003; their Fig. 5), and there are, however, abrupt compositional changes at the transition from the final pegmatite to the hydrothermal stage (Fig. 6 in Thomas et al. 2003). This transition is difficult to reconstruct because rapid changes in P–T may occur below 500°C. A large data set of hydrothermal fluid inclusions (Thomas 1982) has shown that boiling occurred during their entrapment between about 480 and 400°C, typical for the roof of shallow intrusions. A complex interplay between open- and closed-system behavior builds up due to pressure fluctuations from lithostatic to hydrostatic and back to lithostatic, thus producing fluids of different compositions and densities. At this late stage, hydrothermal convection cells may be generated where meteoric waters are introduced and mixed with magmatic fluids (e.g., Sheppard 1994; Thomas et al. 2003).

The gradual transition from pegmatitic to early hydrothermal and the subsequent enrichment and depletion in late hydrothermal fluids of the trace elements Rb, Sn, Cu, and Zn are illustrated in Figs. 7, 8, 9 and 10. As shown above, Rb concentrations are up to several thousands of parts per million when pegmatite melts initially form and decrease down to about 100 ppm at 500°C, due to effects of silicate crystallization and brine exsolution. Rubidium concentrations in associated brines are relatively low. After the termination of the pegmatitic stage below 500°C, Rb concentrations increase in early hydrothermal fluids. Fluids are further enriched in Rb when boiling occurs and salinities increase at 400 to 450°C. Rubidium concentrations drop to lower values at the late hydrothermal stage when salinities become low again (Fig. 7, Table 4). Cesium concentrations broadly mimic the behavior of Rb during most stages. However, Cs concentrations continue to increase when the late hydrothermal stage is attained (500 to 2,000 ppm of Cs; Table 4) in contrast to the behavior of Rb.

Initial pegmatite melts contain about 1,600 ppm of Sn. Concentrations decrease dramatically towards lower temperatures due to crystallization of cassiterite I, mainly between 650 and 550°C. While the last pegmatite melts are low in Sn concentrations (64 ppm at 500°C), early hydrothermal fluids again become enriched and attain concentrations of about 800 ppm at the boiling stage. A sudden drop occurs in late hydrothermal fluids (23 ppm at 370°C; Fig. 8, Table 4), resulting from precipitation of cassiterite II between 400 and 370°C. Precipitation of

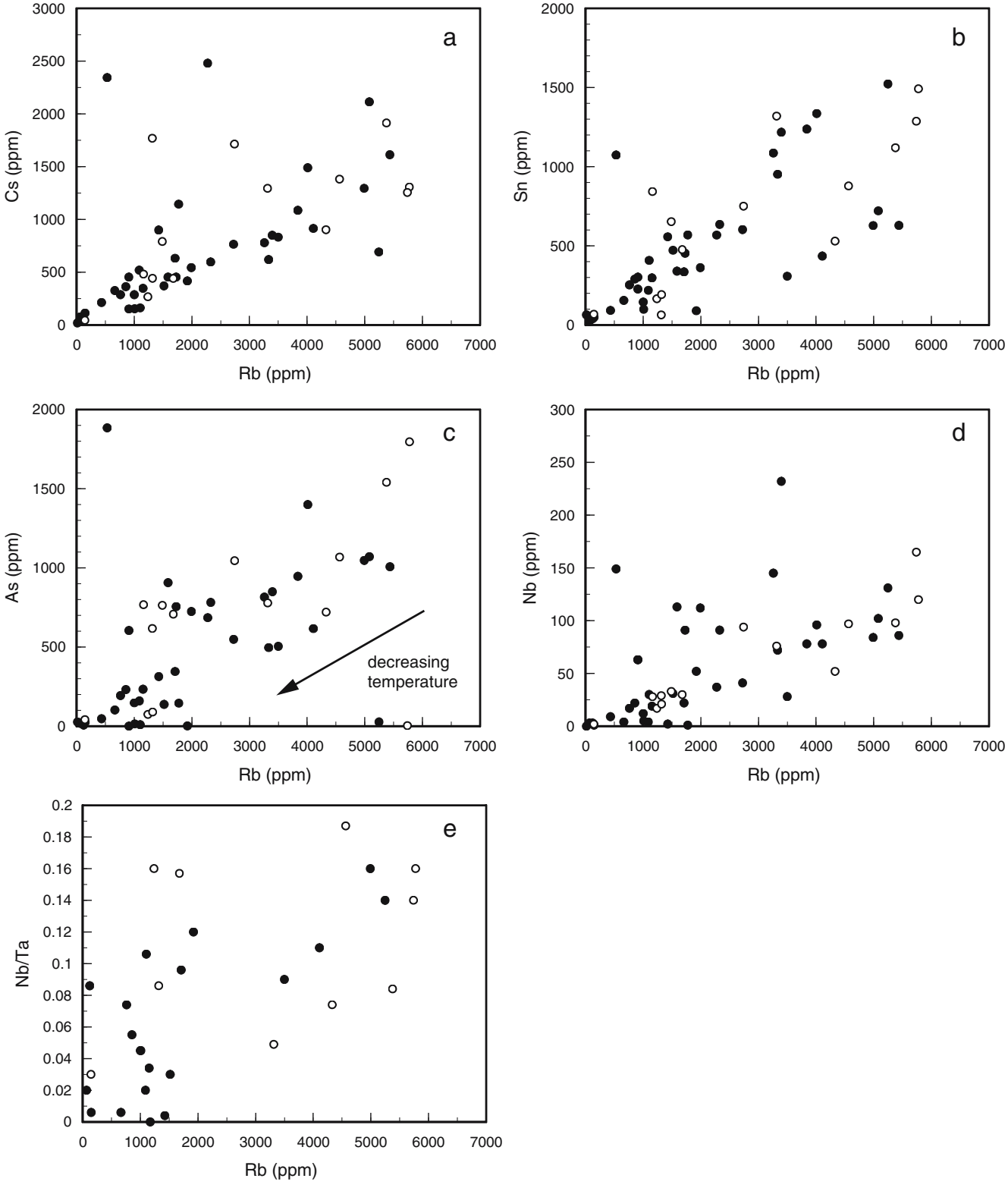

Fig. 6 Plot of Rb concentrations vs **a** Cs, **b** Sn, **c** As, **d** Nb, and **e** Nb/Ta concentrations in type-A (*filled circles*) and type-B (*open circles*) melt inclusions. The *arrow* indicates evolution towards lower temperatures (cf. Fig. 5). Data are from Table 3

cassiterite II dominates the Ehrenfriedersdorf tin ore deposit. This does not necessarily imply that the main quantity of Sn was removed from the melt–fluid system at this stage. Field studies indicate that the majority of cassiterite II rather results from reworked cassiterite I due to dissolution–precipitation processes at late hydrothermal conditions.

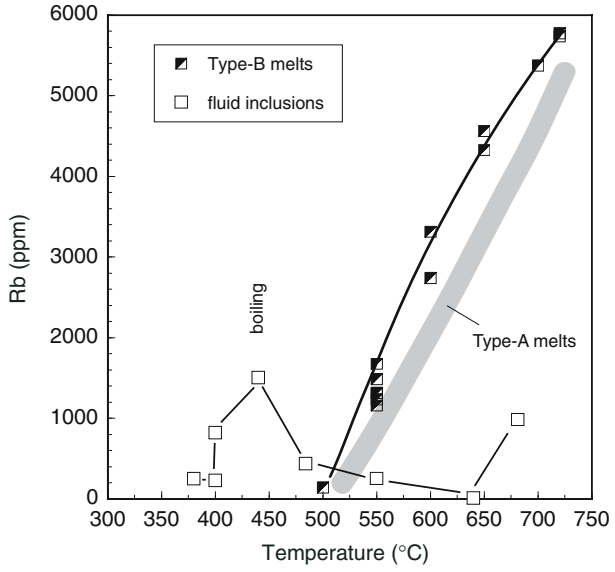

Fig. 7 Rubidium concentrations in type-A and type-B melt and fluid inclusions vs temperature. Data are from Tables 3 and 4

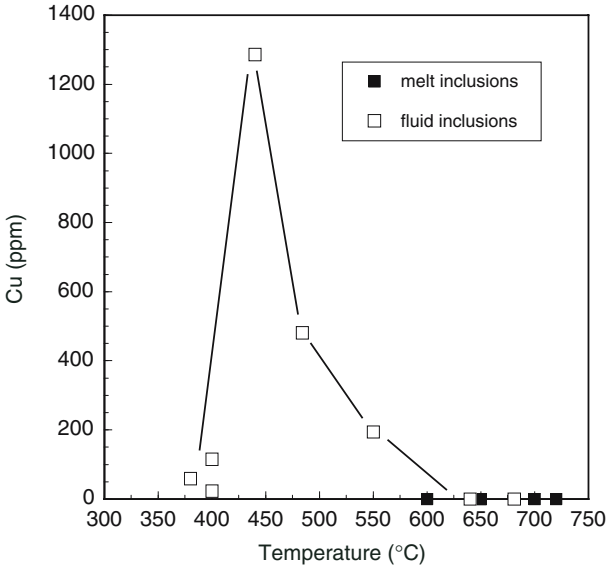

Fig. 9 Copper concentrations in melt and fluid inclusions vs temperature. Data are from Tables 3 and 4

Copper is always below the lower limits of detection in melts and high-temperature brines. It becomes significantly enriched in fluids with about 200 ppm at 550°C, 500 ppm at 480°C, and 1,300 ppm at 440°C, when boiling conditions are attained (Fig. 9). Similar to Sn, concentrations of Cu drop rapidly to values <120 ppm at 400–370°C, due to precipitation of mainly chalcopyrite. Similarly, a concentration increase in early hydrothermal fluids is also seen for As and Sb, with maximum values of 500 and 170 ppm, respectively, at boiling conditions and a decrease at the late hydrothermal stage probably due to concomitant precipitation of arsenopyrite along with chalcopyrite.

Figure 10 shows the progressive increase of Zn during the hydrothermal evolution. Concentrations at the pegmatite stages are low. Unlike Sn and Cu, Zn concentrations continuously increase at the later hydrothermal stage, up to 3,000 ppm at 400°C (Table 4). Precipitation of sphalerite may start at these conditions (Fig. 3), the main removal of Zn from the fluid system, however, occurs at even lower temperatures. This is in line with field observations indicating that formation of sphalerite is not coeval with that of cassiterite II, but later. There is similar strong enrichment of Fe from early (up to 1,000 ppm) to late hydrothermal fluids (up to 8,000 ppm; Table 4). The

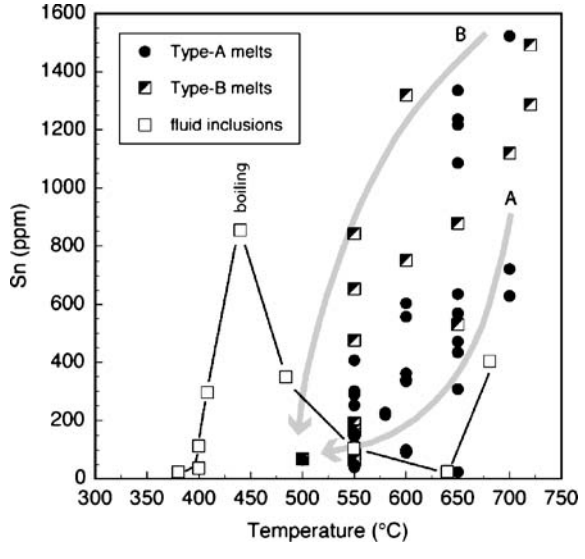

Fig. 8 Tin concentrations in type-A and type-B melt and fluid inclusions vs temperature. *Arrows* tentatively trace the evolution of both melt types, indicating overall enrichment of Sn in type-B melts. Data are from Tables 3 and 4, with the exception of one fluid inclusion at 410°C (308 ppm Sn), which is from Thomas et al. (2003)

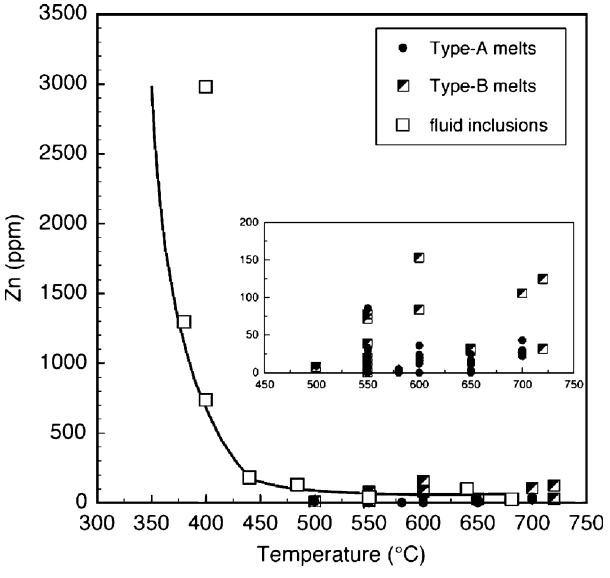

Fig. 10 Zinc concentrations in type-A and type-B melt and fluid inclusions vs temperature. *Inset* is a blow-up of Zn concentrations for both melt types at low Zn contents and shows the relative enrichment of Zn in type-B, relative to type-A melts. Data are from Tables 3 and 4

concomitant enrichment of Zn and Fe is reflected in the compositions of sphalerite. Early ZnS that precipitated at about 380°C is Fe-poor. Late sphalerite precipitated between 350 and 300°C is extremely Fe-rich with Fe/Zn ratios of about 0.33.

Thus, melt and fluid inclusions trace the evolution of the mineralizing pegmatites and hydrothermal fluids at Ehrenfriedersdorf. Melt and fluid inclusion concentrations of the elements Sn, Cu, and Zn directly reflect the crystallization and precipitation history of ore-forming minerals at distinctive temperatures or temperature windows. The SXRF data set does not allow for clarification of the behavior of W at Ehrenfriedersdorf. At the moment, we have no explanation for this behavior.

Conclusions

The trace element behavior of the H_2O-, B- and F-rich granite–pegmatite–hydrothermal system at the Variscian Ehrenfriedersdorf Complex, Germany, was studied using single melt and fluid inclusions of a well-characterized sample set. The results presented in this study complement results published in earlier studies of Thomas et al. (2003) adding important information on trace elements. By a combination of selected microanalytical techniques (rehomogenization experiments, Raman spectroscopy, SXRF, and optical microscopy) the sequence and relation of the inclusions and trace element compositions were determined for selected single inclusions, allowing a detailed study of the trace element evolution of the complex system. The SXRF analysis of daughter crystals in inclusions (water-rich melts and fluids) in combination with Raman spectroscopy enables quantitative analysis of dilute and heterogeneously distributed elements in the melts and fluids.

Quantitative results on melt inclusions show a decrease of most trace elements with ongoing fractional crystallization, i.e., with falling temperature. During the pegmatite-stage melt immiscibility process generating coexisting type-A and type-B melts, most trace elements are preferentially fractionated into the water-rich type-B melts. Fluid phases exsolve from the melts during the pegmatite stage and are already enriched in economically important elements like Sn and Cu and in Rb. The largest compositional variations occur during the hydrothermal stage: two stages of strong Sn enrichment followed by a significant Zn enrichment are documented. These findings are well in accordance with the occurrence of two genetically different cassiterite deposits at Ehrenfriedersdorf, as well as later-stage sphalerite. Homogenization temperatures revealed that precipitation of cassiterite I took place between 650 and 550°C. A second phase of cassiterite separation is correlated with a drop in Sn concentrations in the fluids observed at 400 and 370°C. Zinc precipitation was shown to take place at even lower temperatures around 300°C. The behavior of W is more difficult to unravel, with concentrations mostly below the lower limits of detection. When W was present, it was detected in all kinds of inclusions at variable concentrations. Thus, the data at the present stage do not give a clear result, and the enrichment process of W at Ehrenfriedersdorf must await further studies.

It was shown in this study that SXRF is a useful method to observe the enrichment and decoupling of elements during the evolution of a magmatic system on the basis of quantitative, single-inclusion analysis. The combined analysis of daughter crystals with Raman spectroscopy has a high potential in detecting dilute elements on the one hand, but also in finding constraints on anionic species responsible for element transportation at high temperatures. We believe that the study of the speciation of trace elements during transportation and boiling processes is one major subject in the next few years, and one important and straightforward method to advance this is a combination of SXRF and Raman spectroscopy.

Acknowledgements The authors thank Christian Schmidt, Volker Lüders, Ilya Veksler, Max Wilke, Gerald Falkenberg, Laszlo Vincze, and Bart Vekemans for discussions and collaboration during this study. We are grateful to the Hamburger Synchrotronstrahlungslabor for beamtime at beamline L and to the Geoforschungszentrum for support of this study. Editorial handling by Bernd Lehmann and Robert Moritz is highly appreciated. We thank Robert Linnen and Dima Kamenetsky for their constructive and helpful reviews.

References

Anderson AJ, Bodnar RJ (1993) An adaptation of the spindle stage for geometric analysis of fluid inclusions. Am Mineral 78: 657–664

Audétat A, Pettke T (2003) The magmatic-hydrothermal evolution of two barren granites: a melt and fluid inclusion study of the Rito del Medio and Caòada Pinatebe plutons in northern New Mexico (USA). Geochim Cosmochim Acta 67:97–121

Dahm KP, Thomas R (1985) Ein neues Modell zur Genese der Zinnlagerstätten im Erzgebirge (Quarz-Kassiterit-Formation). Freib Forsch.hefte, C 390:254–274

Diamond LW (2001) Review of the systematics of CO_2-H_2O fluid inclusions. Lithos 55:69–99

Falkenberg G, Rickers K (2002) Pink beam and monochromatic micro-X-ray fluorescence analysis at the beamline L. HASYLAB Annual Report, pp 88–95

Förster HJ, Tischendorf G, Trumbull RB, Gottesmann B (1999) Late collisional granites in the Variscan Erzgebirge, Germany. J Petrol 40:1613–1645

Kamenetsky VS, van Achterbergh E, Ryan CG, Naumov VB, Mernagh TP, Davidson P (2002) Extreme chemical heterogeneity of granite-derived hydrothermal fluids: an example from inclusions in a single crystal of miarolitic quartz. Geology 30:459–462

Kamenetsky VS, Naumov VB, Davidson P, van Achterbergh E, Ryan CG (2004) Immiscibility between silicate magmas and aqueous fluids: a melt inclusion pursuit into the magmatic-hydrothermal transition in the Omsukchan Granite (NE Russia). Chem Geol 210:73–90

Lechtenberg F, Garbe S, Bauch J, Dingwell DB, Freitag J, Haller M, Hansteen TH, Ippach P, Knöchel A, Radke M, Romano C, Sachs PM, Schmincke HU, Ullrich HJ (1996) The X-ray fluorescence measurement place at beamline L of Hasylab. J Trace Microprobe Tech 14:561–587

Linnen RL (1998) The solubility of Nb-Ta-Zr-W in granitic melts with Li and Li+F: constraints for mineralization in rare metal granites and pegmatites. Econ Geol 93:1013–1025

Linnen RL, Keppler H (1997) Columbite solubility in granitic melts: consequences for the enrichment and fractionation of Nb and Ta in the Earth's crust. Contrib Mineral Petrol 128:213–227

London D (1992) The application of experimental petrology to the genesis and crystallization of granitic pegmatites. Can Mineral 30:499–540

London D (1999) Melt boundary layers and the growth of pegmatite textures. Can Mineral 37:826–827

Lowenstern JB (2003) Melt inclusions come of age: volatiles, volcanoes, and Sorby's legacy. In: De Vivo B, Bodnar RJ (eds) Melt inclusions in volcanic systems—methods, applications and problems. Elsevier, Amsterdam, pp 1–21

Naumov VB (1979) Determination of concentration and pressure of volatiles in magmas from inclusions in minerals. Geochem Int 16:33–40

Rickers K, Thomas R, Heinrich W (2004) Trace-element analysis of individual synthetic and natural fluid inclusions with synchrotron radiation XRF using Monte Carlo simulations for quantification. Eur J Mineral 16:23–35

Roedder E (1984) Fluid inclusions. Reviews in mineralogy, vol 12. Mineralogical Society of America, Washington, DC, p 644

Roedder E (1992) Fluid inclusion evidence for immiscibility in magmatic differentiation. Geochim Cosmochim Acta 56:5–20

Roedder E (2003) Significance of melt inclusions. In: De Vivo B, Bodnar RJ (eds) Melt inclusions in volcanic systems — methods, applications and problems. Elsevier, Amsterdam, pp XV–XVII

Sheppard SMF (1994) Stable isotope and fluid inclusion evidence for the origin and evolution of Hercynian mineralizing fluids. In: Seltmann R, Kämpf H, Möller P (eds) Metallogeny of collisional orogens. Czech Geological Survey, Prague, pp 49–60

Thomas R (1982) Ergebnisse der thermobarogeochemischen Untersuchungen an Flüssigkeitseinschlüssen in Mineralen der postmagmatischen Zinn-Wolfram-Mineralisation des Erzgebirges. Freib Forsch.hefte, C 370:1–85

Thomas R (2000) Determination of water contents of granite melt inclusions by confocal laser Raman microprobe spectroscopy. Am Mineral 85:868–872

Thomas R (2002) Determination of the H_3BO_3 concentration in fluid and melt inclusions in granite pegmatites by laser Raman microprobe spectroscopy. Am Mineral 87:56–68

Thomas R, Webster JD (2000) Strong tin enrichment in a pegmatite-forming melt. Miner Depos 35:570–582

Thomas R, Webster JD, Heinrich W (2000) Melt inclusions in pegmatite quartz: complete miscibility between silicate melts and hydrous fluids at low pressure. Contrib Mineral Petrol 139:394–401

Thomas R, Webster JD, Rhede D, Seifert W, Rickers K, Förster HJ, Heinrich W, Davidson P (2006) The transition from peraluminous to peralkaline granitic melts: evidence from melt inclusions and accessory minerals. Lithos (in press)

Thomas R, Förster HJ, Heinrich W (2003) The behaviour of boron in a peraluminous granite-pegmatite system and associated hydrothermal solutions: a melt and fluid-inclusion study. Contrib Mineral Petrol 144:457–472

Thomas R, Förster HJ, Rickers K, Webster J (2005) Formation of extremely F-rich hydrous melt fractions and hydrothermal fluids during differentiation of highly evolved tin-granite magmas: a melt/fluid inclusion study. Contrib Mineral Petrol 148:582–641

van Espen P, Janssens K, Swenters I (1992) AXIL X-ray analysis software. Manual and computer program. University of Antwerp, Antwerp

Vekemans B, Janssens K, Vincze L, Adams F, van Espen P (1995) Comparison of several background compensation methods useful for evaluation of energy-dispersive X-ray fluorescence spectra. Spectrochim Acta B Atom Spectrosc 50:149–169

Vekemans B, Janssens K, Vincze L, Adams F, van Espen P (2004) Analysis of X-ray spectra by iterative least squares (AXIL): new developments. X-ray Spectrom 23:278–285

Veksler IV, Dorfman AM, Dingwell DB, Zotov N (2002a) Element partitioning between immiscible borosilicate liquids: a high-temperature centrifuge study. Geochim Cosmochim Acta 66:2603–2614

Veksler IV, Thomas R, Schmidt C (2002b) Experimental evidence of three coexisting immiscible fluids in synthetic granitic pegmatite. Am Mineral 87:775–779

Vincze L, Janssens K, Adams F (1993) A general Monte Carlo simulation of energy-dispersive X-ray fluorescence spectrometers — part I. Spectrochim Acta B Atom Spectrosc 48: 553–573

Vincze L, Janssens K, Adams F, Rindby A (1995a) A detailed ray-tracing code for capillary X-ray optics. X-ray Spectrom 24: 27–37

Vincze L, Janssens K, Adams F, Rivers ML, Jones KW (1995b) A general Monte Carlo simulation of energy-dispersive X-ray fluorescence spectrometers — part II. Spectrochim Acta B Atom Spectrosc 50:127–148

Vincze L, Janssens K, Adams F, Jones, KW (1995c) A general Monte-Carlo simulation of energy dispersive X-ray fluorescence spectrometers — part III. Spectrochim Acta B Atom Spectrosc 50:1481–1500

Webster JD, Thomas R, Rhede D, Förster H-J, Seltmann R (1997) Melt inclusions in quartz from an evolved peraluminous pegmatite: geochemical evidence for strong tin enrichment in fluorine-rich and phosphorus-rich residual liquids. Geochim Cosmochim Acta 61:2589–2604

Webster JD, Thomas R, Förster HJ, Seltmann R, Tappen C (2004) Geochemical evolution of halogen-enriched, granite magmas and mineralising fluids of the Zinnwald tin-tungsten mining district, Erzgebirge, Germany. Miner Depos 39:452–472